Robust bound state in the continuum in a nonlinear microcavity embedded in a photonic crystal waveguide

E. N. Bulgakov and A. F. Sadreev*

L.V. Kirensky Institute of Physics, Siberian Branch of Russian Academy of Sciences, 660036, Krasnoyarsk, Russia
**Corresponding author: almas@tnp.krasn.ru*

Received June 26, 2014; accepted July 26, 2014;
posted July 31, 2014 (Doc. ID 214597); published August 29, 2014

We present a two-dimensional photonic crystal design of four defect dielectric rods, which form a microcavity with eigenfrequencies residing in the propagating band of a directional waveguide. In this system, a nonrobust bound state in the continuum (BSC) occurs as a result of full destructive interference of the monopole and quadrupole modes, with the same parity at certain values of the material parameters of the defect rods. Due to the Kerr effect, a robust BSC arises in a self-adaptive way without necessity to tune the material parameters. The absence of the superposition principle in that nonlinear system gives rise to coupling of the BSC with injected light, resulting in a novel transmission resonance. © 2014 Optical Society of America

OCIS codes: (190.3270) Kerr effect; (190.5940) Self-action effects; (230.5298) Photonic crystals.
http://dx.doi.org/10.1364/OL.39.005212

In 1929, von Neumann and Wigner [1] predicted the existence of discrete solutions of the single-particle Schrödinger equation, which are embedded in the continuum of positive energy states; thus, bound states in the continuum (BSC). For a long time, their analysis was regarded as mathematical curiosity because of certain spatially oscillating central symmetric potentials. That situation cardinally changed when Friedrich and Wintgen [2] in the framework of a two-level Fano–Anderson model formulated the BSC as a resonant state whose width tends to zero, since at least one physical parameter varies continuously (see [3–5]). Localization of the resonant states in an open system, i.e., the BSC, can be considered a result of destructive interference of two resonance states, which occur at their avoided crossing [2,5]. This is accompanied by one of the resonant states transforming into a trapped state with a vanishing width, while the other acquires the maximal resonance width (super-radiant state [3,5]).

Similar to the Anderson localization, the BSC phenomenon is a manifestation of wave interference and is generic to all wave phenomenon. In particular, Shipman and Venakides [6] predicted symmetry-protected trapping of electromagnetic waves in the periodical array of dielectric rods. Two theoretical groups independently presented examples of the BSC in photonics [7–9], exploiting the Fabry–Perot mechanism [10–13]. Subsequently, such photonic BSCs were observed experimentally [14–17]. Realization of the BSC in the 1D PhC by the advanced digital grading method was described in [18]. The trapping of waves due to destructive interference also was considered in water waves and acoustics [19,20].

In this Letter, we present a PhC design of in-channel optical microcavity embedded into the waveguide and show that it is capable to realize the BSC, as the result of destructive interference of two resonant modes with the same parity. This generic mechanism of the trapping of waves [2,5] is novel in photonics. However, in linear open systems, the BSC occurs at the unique singular point in the parameter space [3,5]. This constitutes a difficulty for experimental observation of the BSC in photonics. First, it is necessary to vary the parameters of the microcavity in order to approach the BSC point. Second, the BSC is decoupled from the waveguide continuum [5,21]; therefore, the BSC cannot be directly probed by a wave incoming from the waveguide. We show that the nonlinear Kerr effect removes this difficulty. The BSC appears in a self-adaptive way due to the nonlinear shift of the dielectric constant [22,23], which transforms the BSC point into a line in the space of frequency and dielectric constant. The nonlinearity breaks the superposition principle to give rise to interaction between the injected wave and the BSC. Therefore, incoming light excites the BSC and forms a complicated response picture, which is crucially different from the Breit–Wigner or Fano resonances.

The PhC system layout is shown in Fig. 1, with all parameters given in the caption. The single row of rods is removed from the PhC to form a directional photonic waveguide, which supports a single-band-guided TM mode spanning from the bottom band edge 0.315 to the upper one 0.41 in terms of $2\pi c/a$ [24], where a is the lattice unit. The TM mode has the electric field component parallel to the infinitely long rods. Four linear defect rods of the same radius with dielectric constant ϵ, shown by green open circles, are placed at the vertexes of a square. These four defect rods form an optical microcavity

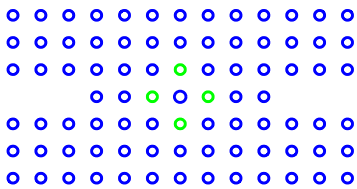

Fig. 1. PhC consists of a square lattice of GaAs rods with a linear refractive index $n_0 = 3.4$ and nonlinear refractive index $n_2 = 1.5 \times 10^{-13}$ cm^2/W at $\lambda = 1.55\,\mu$m and radius $0.18a$ in air, as shown by blue open circles, where a is the lattice unit. Four linear defect rods of the same radius with dielectric constant ϵ are shown by green circles.

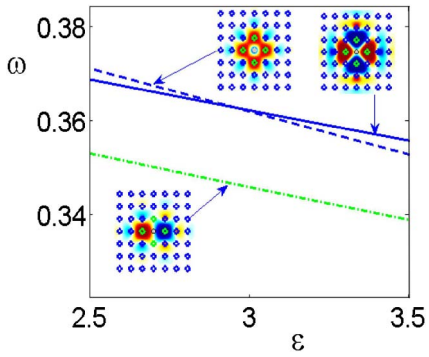

Fig. 2. Eigenfrequencies in units of $2\pi c/a$ versus dielectric constant of the microcavity. Insets show profiles of the eigenmodes.

embedded into the PhC waveguide. On both sides of the microcavity, additional rods are inserted in the waveguide in order to increase the Q factor of the microcavity.

The eigenfrequencies of the cavity versus the dielectric constant ϵ are plotted in Fig. 2 together with the eigenmodes [24]. The eigenfrequencies of the monopole and quadrupole-diag modes cross, while two degenerate dipole modes have a negligible effect on the BSC. The quadrupole x–y mode has an eigenfrequency beyond the propagation band of the PhC waveguide within the chosen range of ϵ.

We study the light trapping in the microcavity by numerically solving the Maxwell equations and by means of the coupled mode theory. The former approach is based on the Lippmann–Schwinger equation [25]:

$$[\hat{H}_{\text{eff}} - \omega^2]\psi_S = \hat{\Gamma}\psi_{\text{in}}, \tag{1}$$

where $\hat{H}_{\text{eff}}$ is the non-Hermitian effective Hamiltonian obtained by projection of the total space of the PhC system onto the inner space of the microcavity. In this approach, the scattering function ψ_S is the electric field, while the right-hand term in Eq. (1) accounts for the coupling of injected light ψ_{in} with the microcavity through the coupling matrix $\hat{\Gamma}$. The BSC occurs when the inverse of the matrix $H_{\text{eff}} - \omega^2$ does not exist. Calculations show that the BSC point is achieved at $\epsilon_{\text{BSC}} = 3.00456$, $\omega_{\text{BSC}} = 0.36183$. In the linear system, the BSC is the eigenfunction of the effective Hamiltonian with a real eigenvalue and, thus, is decoupled from the continuum [5,21]. Nevertheless, the BSC could be found in the parametric space as a special point, where the line of zero transmittance $t = 0$ touches the unit transmittance $|t| = 1$ [5]. At this point, the collapse of the Fano resonance takes place [10], as shown in Fig. 3(b). One can see from Fig. 4 that, approaching the BSC point along the line $|t| = 1$, the scattering wave function converges to the BSC, provided that the parameter ϵ is close to the BSC point ϵ_{BSC}. Note, although the scattering state in Fig. 4(b) is very close to the BSC in Fig. 4(c), the localized BSC does not support power flows.

Numerically, the dimension of the inner space of the microcavity is around thousands of sites per elementary cell in the finite difference scheme. The numerical analysis can be enormously simplified if only two relevant eigenmodes, monopole, and quadrupole-diag are taken

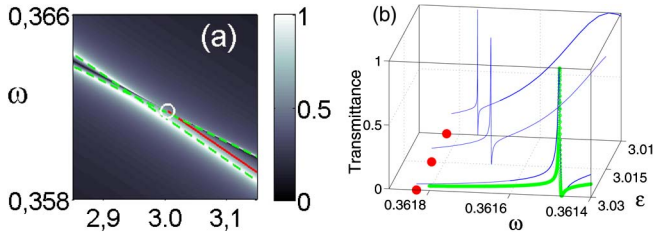

Fig. 3. (a) Transmittance versus frequency of injected light and dielectric constant of the defect rods in the two-level approximation. The BSC point is marked by the white open circle. It is seen that the Kerr effect transforms the BSC point into a line (red). (b) Transmittance versus frequency in the vicinity of the BSC point. The three slices correspond to $\epsilon = 3.03$, 3.015, 3.01. Red closed circles mark the BSC frequency. Results of computation based on the Maxwell equations are shown by green open circles, while the CMT results are shown by solid blue lines.

into consideration. That decimation procedure corresponds to the coupled mode theory (CMT) if the radiation shifts in the effective Hamiltonian are neglected [7,25,26]. The CMT equations take the following form:

$$[H^{(2)}_{\text{eff}} - \omega]\begin{pmatrix} A_1 \\ A_2 \end{pmatrix} = -i\begin{pmatrix} \sqrt{\gamma_1} \\ \sqrt{\gamma_2} \end{pmatrix}\psi_{\text{in}}, \tag{2}$$

where

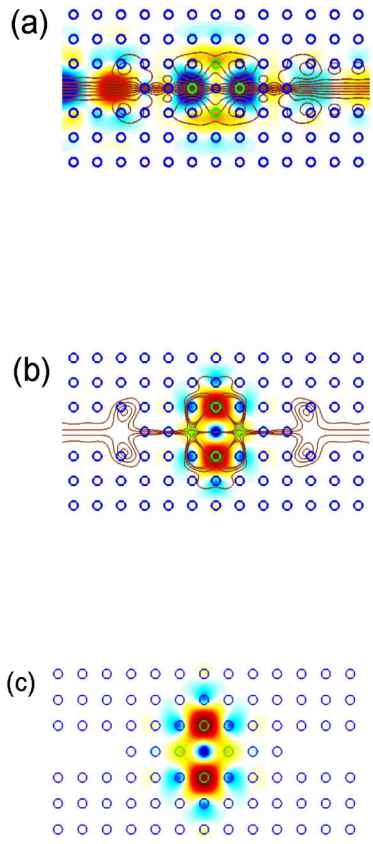

Fig. 4. Solutions of Eq. (1) (real parts) for (a) $\epsilon = 3.01$, $\omega = 0.3619$ and (b) $\epsilon = 3.01$, $\omega = 0.361755$. Thin solid lines show the Poynting vector flow lines. (c) BSC.

$$H_{\text{eff}}^{(2)} = \begin{pmatrix} \omega_1 - i\gamma_1 & -u - i\sqrt{\gamma_1\gamma_2} \\ -u - i\sqrt{\gamma_1\gamma_2} & \omega_2 - i\gamma_2 \end{pmatrix}; \quad (3)$$

the subscripts 1 and 2 refer to the monopole and quadrupole-diag eigenmodes. We approximate their eigenfrequencies as $\omega_{1,2} = \omega_0 \pm \Delta$, where the parameters were found numerically from the Maxwell equations $\Delta = 0.0025367(\epsilon - 2.9518)$, $\omega_0 = 0.362443 - 0.01567683(\epsilon - 2.9518)$, $\gamma_1 = 3 \cdot 10^{-5}$, $\gamma_2 = 1.3 \cdot 10^{-4}$, and $u = 1.768583 \cdot 10^{-4}$. The amplitude of transmittance is given by [7,26]

$$t = \psi_{\text{in}} + \sqrt{\gamma_1}A_1 + \sqrt{\gamma_2}A_1 \quad (4)$$

and is shown in Fig. 3.

The transmittance presented in Fig. 3(b) demonstrates good agreement between the CMT approximation and the numerical solution of the Maxwell equations. In the framework of the CMT approach, the BSC point can be found analytically [3,5]:

$$\omega_2 - \omega_1 = \frac{u(\gamma_2 - \gamma_1)}{\sqrt{\gamma_1\gamma_2}}, \qquad \omega_{\text{BSC}} = \omega_2 + u\sqrt{\frac{\gamma_2}{\gamma_1}}. \quad (5)$$

The above consideration of the linear PhC system shows that occurrence of the BSC demands fine tuning of the material parameter (dielectric constant or diameter) of the defect rods in order to satisfy the equation for the BSC point in Eq. (5). Therefore, probing the BSC in light transmission by injecting light of a monochromatic laser is an experimental challenge. We show that the Kerr effect can remove this problem, making the BSC point self-adaptive [22,23].

In the vicinity of the BSC point, the light intensity is sufficiently large only in the microcavity. Therefore, we can neglect the Kerr effect outside the microcavity and modify the effective non-Hermittian Hamiltonian as follows [27]: $H_{\text{eff}}^{(2)} \to H_{\text{eff}}^{(2)} + V_{mn}$, where

$$V_{mn} = -\frac{n_0 c^2 n_2^2(\omega_m + \omega_n)}{16\pi a^2} \int \mathrm{d}^2\vec{r}|A_1E_1(\vec{r}) + A_2E_2(\vec{r})|^2 E_m(\vec{r})E_n(\vec{r}) \quad (6)$$

and $E_m(x, y)$ are the monopole and quadrupole-diag eigenmodes of the linear cavity, as shown in Fig. 2. Two factors substantially weaken the nonlinear contribution of the quadrupole-diag mode. First, as seen from Fig. 2, two nodal lines of the quadrupole mode go through the central defect rod. Second, $\gamma_1 \ll \gamma_2$, which suppresses excitation of the quadrupole-diag mode. Thus, one can conclude that only the nonlinear term associated with the monopole mode is important $\omega_1 \to \omega_1 + V_{11} = \omega_1 - \lambda_{11}|A_1|^2$. Then Eq. (5) shows that the BSC point is achieved if the intensity of the monopole mode equals

$$\lambda_{11}I_{1c} = \lambda_{11}|A_1|^2 = \omega_2 - \omega_1 - \frac{u(\gamma_2 - \gamma_1)}{\sqrt{\gamma_1\gamma_2}}, \quad (7)$$

with the BSC frequency defined in Eq. (5), as in the linear case. The BSC is given by equation $\text{Det}[H_{\text{eff}}^{(2)} - \omega_{\text{BSC}}] = 0$.

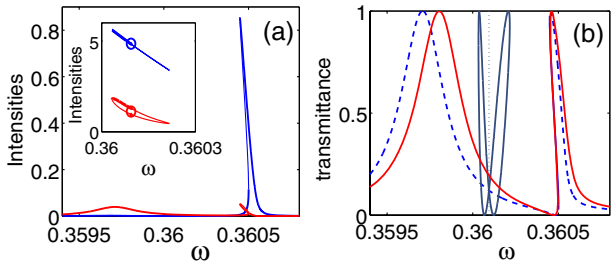

Fig. 5. (a) Intensities of the monopole mode $|A_1|^2$ (blue lines) and quadrupole-diag mode $|A_2|^2$ (red lines) for $\lambda_{11} = 10^{-4}$ and $\epsilon = 3.1$. Thin lines correspond to unstable solutions, while thicker lines show stable solutions. (b) Transmittance versus frequency of injected light with the amplitude $\psi_{\text{in}} = 0.0025$. Blue dash lines show transmittance found from the nonlinear CMT equations, and red solid lines show transmittance found from nonlinear Maxwell equations.

Moreover, the second equation in Eq. (2) gives an equality $(\omega_{\text{BSC}} - \omega_2 + i\gamma_2)A_2 + (u + i\sqrt{\gamma_1\gamma_2})A_1 = 0$, which defines the intensity of the quadrupole-diag mode at the BSC point:

$$I_{2c} = |A_{2c}|^2 = \frac{\gamma_1}{\gamma_2}I_{1c}. \quad (8)$$

Intensities at the BSC are marked in Fig. 5(a) by open circles.

After substitution of the nonlinear term $\omega_1 \to \omega_1 - \lambda_{11}|A_1|^2$ into Eq. (3) and solving the nonlinear equations, we obtain two different families of solutions [23]. The first family inherits the linear case and, at low injected power, has typical resonance behavior of the mode intensities $|A_1|^2$, $|A_2|^2$, as shown in Fig. 5(a) in the basic window. The mode (monopole) with the smaller resonant width is excited with a larger amplitude, and the associated resonant peak is shifted more to the left because of the negative contribution of the nonlinear term. The second family of solutions are loops centered at the BSC point in Eq. (7), as shown in the inset of Fig. 5(a). The stability of the solutions are notified by thicker lines. When the amplitude of the injected light ψ_{in} tends to zero, the size of the loops shrinks to the BSC points marked by open circles. The transmittance calculated by Eq. (4) is plotted in Fig. 5(b) for both families and clearly follows the frequency behavior of the intensities shown in Fig. 5(a). The transmittance computed on the basis of the full-fledged nonlinear Maxwell equations is plotted in Fig. 5(b) by a solid red line to demonstrate good agreement with the CMT.

Thus, the PhC design presented in Fig. 1 is capable of realizing the BSC due to destructive interference of the monopole and quadrupole-diag modes decaying into the waveguide. However, in the linear case, this effect demands fine tuning of the material parameters of the defect rods in the microcavity, thereby making the BSC nonrobust. The Kerr effect in the microcavity transforms the BSC point into the line, as shown in Fig. 3(a). According to the terminology proposed in [6], we term such BSC the robust BSC. Second, the nonlinearity gives rise to interaction of the incident wave with the BSC, which results in a new type of loop-shaped resonance, as shown in Fig. 5, which was first shown in [23].

The work was supported by the Russian Science Foundation, grant 14-12-00266. We acknowledge discussions with Chia Wei Hsu and D. N. Maksimov.

References

1. J. von Neumann and E. Wigner, Phys. Z. **30**, 465 (1929).
2. H. Friedrich and D. Wintgen, Phys. Rev. A **32**, 3231 (1985).
3. A. Volya and V. Zelevinsky, Phys. Rev. C **67**, 054322 (2003).
4. M. L. Ladron de Guevara, F. Claro, and P. A. Orellana, Phys. Rev. B **67**, 195335 (2003).
5. A. F. Sadreev, E. N. Bulgakov, and I. Rotter, Phys. Rev. B **73**, 235342 (2006).
6. S. P. Shipman and S. Venakides, Phys. Rev. E **71**, 026611 (2005).
7. E. N. Bulgakov and A. F. Sadreev, Phys. Rev. B **78**, 075105 (2008).
8. D. C. Marinica, A. G. Borisov, and S. V. Shabanov, Phys. Rev. Lett. **100**, 183902 (2008).
9. R. F. Ndangali and S. V. Shabanov, J. Math. Phys. **51**, 102901 (2010).
10. C. S. Kim, A. M. Satanin, Y. S. Joe, and R. M. Cosby, Phys. Rev. B **60**, 10962 (1999).
11. S. Fan, P. R. Villeneuve, J. D. Joannopoulos, M. J. Khan, C. Manolatou, and H. A. Haus, Phys. Rev. B **59**, 15882 (1999).
12. I. Rotter and A. F. Sadreev, Phys. Rev. E **69**, 066201 (2004).
13. I. Rotter and A. F. Sadreev, Phys. Rev. E **71**, 046204 (2005).
14. T. Lepetit, E. Akmansoy, J.-P. Ganne, and J.-M. Lourtioz, Phys. Rev. B **82**, 195307 (2010).
15. Y. Plotnik, O. Peleg, F. Dreisow, M. Heinrich, S. Nolte, A. Szameit, and M. Segev, Phys. Rev. Lett. **107**, 183901 (2011).
16. G. Corrielli, G. Della Valle, A. Crespi, R. Osellame, and S. Longhi, Phys. Rev. Lett. **111**, 220403 (2013).
17. C. W. Hsu, B. Zhen, J. Lee, S.-L. Chua, S. G. Johnson, J. D. Joannopoulos, and M. Soljačić, Nature **499**, 188 (2013).
18. N. Prodanovic, V. Milanovic, and J. Radovanovic, J. Phys. A **42**, 415304 (2009).
19. C. M. Linton and P. McIver, Wave Motion **45**, 16 (2007).
20. S. Hein, W. Koch, and L. Nannen, J. Fluid Mech. **692**, 257 (2012).
21. E. N. Bulgakov, K. N. Pichugin, A. F. Sadreev, and I. Rotter, JETP Lett. **84**, 430 (2006).
22. M. I. Molina, A. E. Miroshnichenko, and Yu. S. Kivshar, Phys. Rev. Lett. **108**, 070401 (2012).
23. E. N. Bulgakov and A. F. Sadreev, Phys. Rev. B **80**, 115308 (2009); ibid 81, 115128 (2010).
24. K. Busch, S. F. Mingaleev, A. Garcia-Martin, M. Schillinger, and D. Hermann, J. Phys. Condens. Matter **15**, R1233 (2003).
25. E. N. Bulgakov and A. F. Sadreev, Phys. Rev. B **86**, 075125 (2012).
26. W. Suh, Z. Wang, and S. Fan, IEEE J. Quantum Electron. **40**, 1511 (2004).
27. E. N. Bulgakov and A. F. Sadreev, Opt. Lett. **39**, 1787 (2014).